Synthesising and Comparing the Microplastic Degradation Efficiencies of Magnetically Removable Bismuth Based Microswimmers

Chua Wenzheng Frederic (Cai Wenzheng) (4i2), Ng Yu Heng (4i2)

Group 01-03

Abstract

Microplastics, being non-biodegradable, present a critical environmental and biological hazard, impacting a wide array of organisms, including humans. However, microswimmers have been shown as a promising area of research to combat these problems by degrading these microplastics, although the efficiencies of microswimmers may differ widely. Hence, this study aims to synthesise and evaluate bismuth-based microswimmers to determine their efficiency in degrading commonly encountered plastic types such as polyvinyl chloride and polystyrene. Through comparative analysis, this project aims to elucidate the potential of these microswimmers in mitigating microplastic pollution, contributing to the development of effective environmental remediation strategies. Characterisation of microswimmers were conducted before the experimentation process to determine its morphological structure and band gaps, which assist in the movement and degradation of microplastics. The characterised microswimmers were then able to successfully degrade microplastics of <100μm in a hydrogen peroxide medium, which acts as fuel to aid the propulsion of microswimmers. This study identifies $BiVO_4$ and Bi_2WO_6 to both be comparable microswimmers in terms of their efficiencies in degrading microplastics in water and hydrogen peroxide, with both performing significantly better in terms of degrading microplastics, as compared to decomposition in water only due to the free radicals formed from UV and VIS wavelengths. Thus, both $BiVO_4$ and Bi_2WO_6 microswimmers are promising in terms of their ability to remove microplastics from water through degradation via Advanced Oxidative Processes (AOP).

1. Introduction

Microplastics (MPs), classified as any type of plastic which measures less than 5mm in diameter, have become a major environmental issue, polluting aquatic ecosystems and drinkable water supplies around the world. On top of 150 metric tonnes, close to 10-20 metric tonnes of plastic waste is added every year (Mazhandu et al., 2020, as cited in Kibria et al., 2023). Chia et al. (2021) suggested that littering is the main origin of MPs in global topsoils, directly affecting the

groundwater quality, while greenhouses are the main source of microplastics in South Korea. Sharifinia et al. (2020) stated various detrimental effects MPs had on the reproductive systems of marine animals, including significant reduction in gamete and oocyte quality, fecundity, sperm swimming speed, and quality of offspring, which could potentially pose a threat to the delicate food web. However, global mitigation efforts are no longer able to keep up with the increasing volume of plastic waste (Borrelle et al., 2020).

Advanced oxidative processes (AOPs) have emerged as promising strategies for degradation and elimination of microplastics. Wang et al. (2019) conducted studies on the efficiency of photocatalytic Au@Ni@TiO_2-based micromotors. The microswimmers were able to remove the extracted MPs and random suspended matter collected from Warnow River, achieving about 67% clearage efficiency in pure water. This has proven the potential of microswimmers effectively degrading MPs and improving the quality of drinking water. However, due to the high band gap (3.2eV) of TiO_2 based microswimmers, they are only able to absorb ultraviolet (UV) light, which can be more exhaustive and less practical than microswimmers with a lower band gap. This study proposes a more efficient microswimmer base of $BiVO_4$ and Bi_2WO_6 due to their lower band gap and faster rate of photocatalysis of H_2O_2 fuel, inducing electrophoretic movement (Appendix B).

2. Objectives and Hypotheses

The objective of this study was to investigate the microplastic degradation efficiencies of $BiVO_4$-Fe_3O_4 and Bi_2WO_6-Fe_3O_4 microswimmers in relation to different types of microplastics, specifically polystyrene (PS) and polyvinyl chloride (PVC).

It was hypothesised that the presence of microswimmers would increase the rate of degradation of microplastics in an aqueous medium. However, Bi_2WO_6-Fe_3O_4 would have a higher microplastic degradation efficiency than $BiVO_4$-Fe_3O_4 due to a higher band gap. It was also hypothesised that PS and PVC will have different degradation rates.

3. Materials and Methods

3.1. Precursor Synthesis

V_2O_5 was synthesised via the decomposition of NH_4VO_3 (Sigma Aldrich, purity; 99.0%). 0.1 mol of NH_4VO_3 was placed in an ashing furnace at 500 ^oC to fully decompose NH_4VO_3 into V_2O_5.

$$2NH_4VO_3\,(s) \rightarrow V_2O_5\,(s) + 2NH_3\,(g) + H_2O\,(g)$$

WO_3 was synthesised via the acid reaction between Na_2WO_4 (Sigma Aldrich, purity; 99.0%) and HCl. Excess HCl was added to 0.1 mol of Na_2WO_4. Yellow precipitate was then rinsed.

$$Na_2WO_4\,(s) + 2HCl\,(aq) \rightarrow WO_3\,(s) + 2NaCl\,(aq) + H_2O\,(l)$$

Bi_2O_3 was synthesised via a decomposition of $Bi(OH)_3$ as suggested by Ding et al. (2016), which was synthesised through a reaction between Bi^{3+} and OH^- ions. $Bi(NO_3)_3$ (Sigma Aldrich, purity; 98.0%) was dissolved in 0.05 M HNO_3 such that the molar ratio of $Bi(NO_3)_3$: HNO_3 = 10:3 to obtain a white suspension. Excess of 4 M NaOH was then quickly added to the prepared solution under vigorous stirring, which resulted in the formation of yellow precipitate. The suspension was allowed to stir for 2 h at 90 °C. The precipitate was then collected and rinsed to obtain Bi_2O_3.

3.2. $BiVO_4$ Synthesis by Aqueous Processes

$BiVO_4$ powder was prepared via aqueous processes by stirring $Bi(NO_3)_3{\cdot}5H_2O$ and V_2O_5 at a ratio of 1:2 as suggested by Kudo, Omori and Kato (1999) for 3 days. $Bi(NO_3)_3$ reacts with water to form $BiONO_3$ which then reacts with V_2O_5 and water to form $BiVO_4$ and HNO_3. The collected orange precipitate was then calcined at 400 °C.

3.2. Bi_2WO_6 Synthesis by Solid State Reaction

In a typical method, Bi_2WO_6 was synthesised via solid state reaction between WO_3 and Bi_2O_3. WO_3 and Bi_2O_3 were dissolved in pure ethanol such that the molar ratio of W^{6+} : Bi^{3+} was 1:2. The mixture was then dried and calcined at 650 °C for 4 h.

3.3. Fe_3O_4 Synthesis by Coprecipitation Method

Fe_3O_4 was synthesised via a standard coprecipitation method. $FeCl_3$ and $FeSO_4$ were dissolved in deionised water such that the molar ratio of Fe^{3+} : Fe^{2+} = 2:1. NaOH was then added slowly to the solution until the pH reached 7. Fe_3O_4 was then collected via magnetic decantation.

3.4. Microswimmer-Fe_3O_4 Composites Synthesis

Microswimmers and Fe_3O_4 suspensions were prepared separately with a molar ratio of 2:1 respectively. Under sonication, the Fe_3O_4 suspension was injected dropwise into the

microswimmer suspension. The suspension was then left under constant stirring for 20 mins. The sample was then collected and dried in an oven at 90 ^{o}C for 3 h.

3.5. Characterisation

Spectroscopic studies of prepared $BiVO_4$ and Bi_2WO_6 were measured using FTIR analysis using an FTIR photometer (Bruker, Alpha II) and a UV-Visible spectrophotometer (Shimadzu, UV-1800). The morphologies and microstructures of prepared samples were investigated by scanning electron microscopy (Zeiss). Motion of the microswimmers was captured using a microscope at 100x magnification (Olympus, CX21FS1).

3.6. Construction of Photoreactor

The photoreactor case was constructed using 4 sheets of A3 acrylic measuring 29.7 cm × 42.0 cm and 2 sheets of acrylic measuring 29.7 cm × 29.7 cm. A 800 lm LED light bulb (IKEA, Solhetta) was then fitted to the top of the centre of the photoreactor.

3.7. Microplastic Degradation Experiments

As with the work of Khairudin et al. (2022), Microplastic degradation experiments were carried out in 9.965 mL of pH 7 buffer solution prepared by dissolving 10 mmol of NaH_2PO_4 and 5 mmol of Na_2HPO_4 in 1 L of deionised water. 5 µL of 100 mg/mL of powdered PS and 30 µL of H_2O_2 was then added to the buffer solution in test tubes. Each test tube was then added with 5 mg of each microswimmer. Glass test tubes were then placed in a photoreactor for 120 h, with UV-Visible absorbance measurements taken every 24 h using a spectrophotometer. The same process was then repeated with PVC. Both times a control was prepared without microswimmers.

Results and Discussion

4.1. Synthesis and Characterization of Fe_3O_4

The magnetic properties of Fe_3O_4 was confirmed by placing Fe_3O_4 under the effect of a magnetic field from a permanent magnet. Fe_3O_4 powder was attracted to the magnet, suggesting that it is a magnetic material.

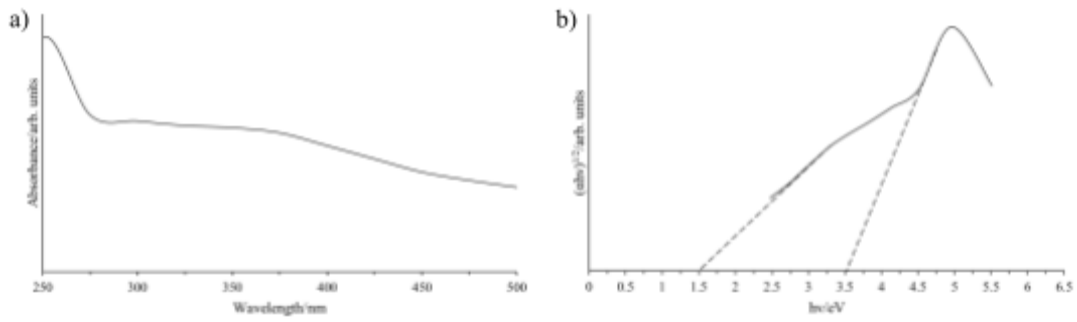

Figure 1. (a) Absorbance Spectra and (b) Tauc Plot for Fe_3O_4 synthesised by coprecipitation.

UV-Vis Spectroscopy was used to identify the band gap of the Fe_3O_4. As shown in Figure 1a, the UV-Vis spectrum of Fe_3O_4 shows a peak at 250 nm. This can be attributed to the excitation of electrons through the bandgap in Fe_3O_4 (Delice et al., 2024). From Figure 1 (a), a Tauc Plot was obtained in Figure 1b by using the Tauc Equation (see Appendix A). The Tauc Plot shows two linear segments, which when extrapolated to the x-axis, shows two values for the band gap, E_g, confirming the E_g of Fe_3O_4 to be between 1.5 to 3.5 eV.

4.2. Synthesis, Characterization and Crystal form of $BiVO_4$ and $BiVO_4/Fe_3O_4$

Synthesis of $BiVO_4$ was based on a series of dissolutions and precipitations. When V_2O_5 and $Bi(NO_3)_3$ were dissolved in water, $Bi(NO_3)_3$ reacted with water to form sparingly soluble $BiONO_3$. Under stirring for 3 days, $BiONO_3$ dissolved and reacted with V_2O_5 to form insoluble $BiVO_4$ which was pale yellow in colour.

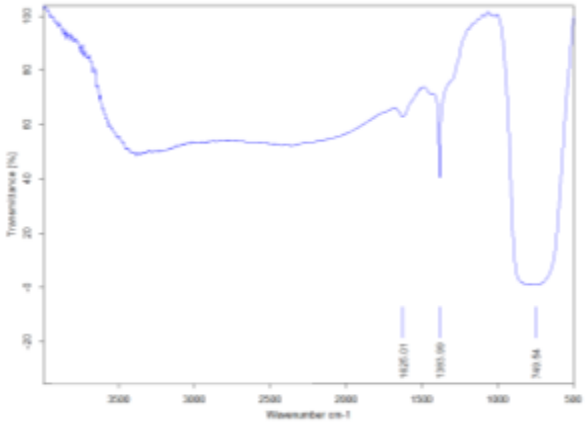

Figure 3. FTIR Spectra of $BiVO_4$ synthesised by aqueous processes.

The FTIR spectrum of $BiVO_4$ nanoparticles (Figure 2) was matched with previously reported $BiVO_4$ FTIR Spectra (Pookmane et al., 2013). The absorption at 749 cm^{-1} is characteristic of an asymmetric stretching and symmetric stretching vibration of the V–O bond. The absorption at 1384 cm^{-1} corresponds to C=O bonds that can be attributed to reactions with atmospheric CO_2 during synthesis while the peak at 1625 cm^{-1} corresponds to the bending vibration of absorbed H_2O molecules.

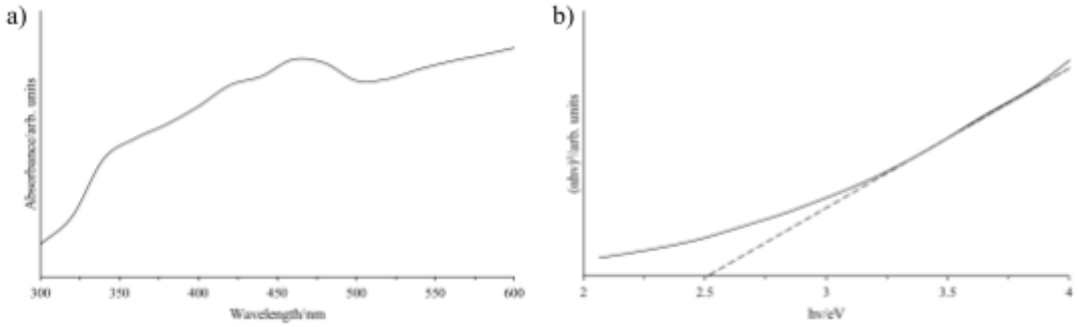

Figure 3. (a) Absorbance Spectra and (b) Tauc Plot for $BiVO_4$ synthesised by aqueous processes.

Figure 3 (b) shows the Tauc Plot of $BiVO_4$ obtained using the absorbance spectra (Figure 2 (a)). The optical band gap was obtained by a linear extrapolation of the linear part of the Tauc Plot, as explained in Appendix A. From the Tauc Plot, an optical band gap of 2.5 eV was obtained, which suggests the successful synthesis of $BiVO_4$ crystals.

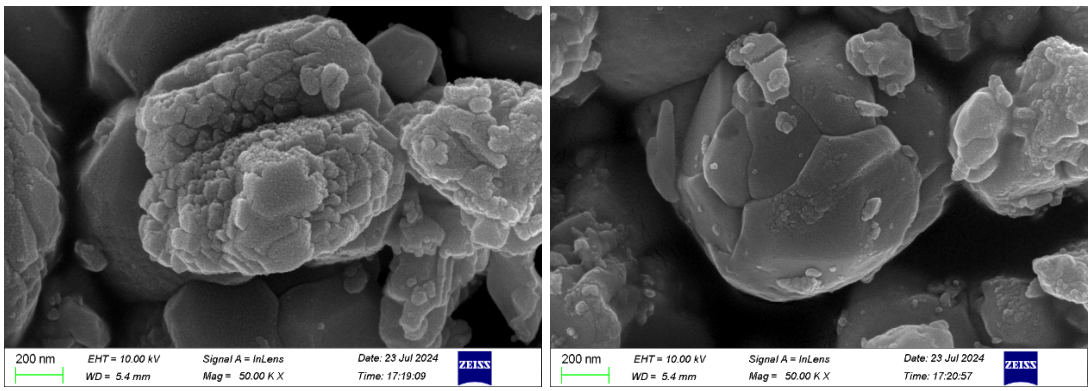

Figure 4. SEM photographs of $BiVO_4$ synthesised via aqueous processes.

The characterisation of the morphology of the $BiVO_4$ microswimmers was done through Scanning Electron Microscopy. Figure 3 confirms that the $BiVO_4$ crystals formed an aggregated

structure with concave and convex surfaces (Yu et al. 2022). The aggregation of $BiVO_4$ crystals can be attributed to the difficulty of optimising reaction kinetics, and the duration of reaction.

Under a microscope, $BiVO_4$ microswimmers were observed to propel themselves, thus confirming the self-propelling nature of the microswimmers.

4.3. Synthesis, Characterization and Crystal form of Bi_2WO_6 and Bi_2WO_6/Fe_3O_4

Synthesis of Bi_2WO_6 was based on a solid state reaction. Under high temperatures, WO_3 and Bi_2O_3 reacted with each other to form Bi_2WO_6, which formed a white powder.

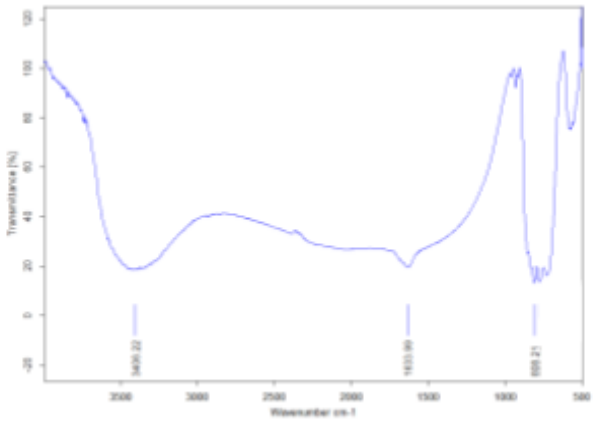

Figure 6. FTIR Spectra of Bi_2WO_6 synthesised by solid state reaction.

The FTIR spectrum of Bi_2WO_6 nanoparticles (Figure 6) was also matched with previously reported Bi_2WO_6 FTIR Spectra (Wang et al., 2021). The absorption at 808 cm^{-1} can be attributed to the stretching vibration of W–O and Bi–O bonds. The wide absorption band at 3406 cm^{-1} corresponds to the stretching vibrations of O–H bonds on the surface of the sample while the peak at 1634 cm^{-1} corresponds to the bending vibration of absorbed H_2O molecules.

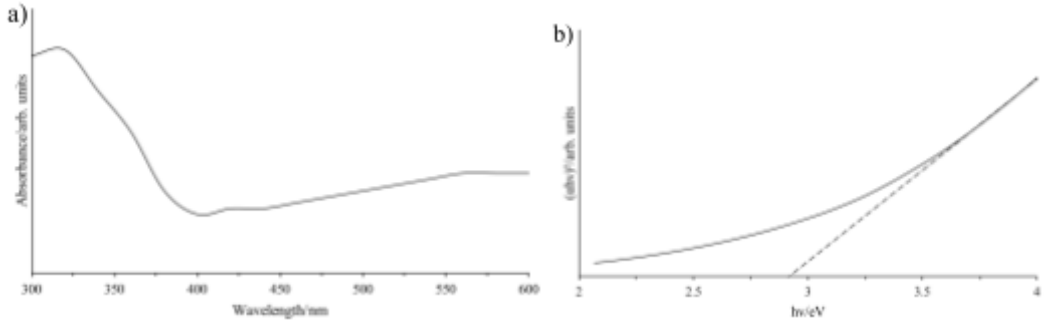

Figure 7. (a) Absorbance Spectra and (b) Tauc Plot for $BiVO_4$ synthesised by aqueous processes.

Figure 7 (b) shows the Tauc Plot of Bi_2WO_6 obtained using the absorbance spectra (Figure 7 (a)). From the Tauc Plot, an optical band gap of 2.8 eV was obtained, which suggests the successful synthesis of Bi_2WO_6 crystals.

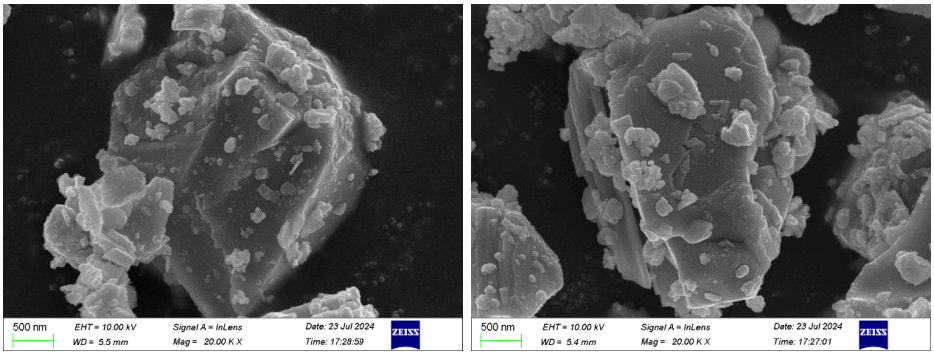

Figure 8. SEM photographs of Bi_2WO_6 synthesised via solid state reaction.

SEM photographs of synthesised Bi_2WO_6 show that Bi_2WO_6 has a larger crystal size which was approximately twice the diameter of the synthesised $BiVO_4$. Less aggregation was observed, which can be attributed to the temperature and duration of synthesis being maintained as suggested by existing literature (Liu et al., 2019).

Similarly, Bi_2WO_6 microswimmer motion was characterised via observations under magnification of a microscope. Self-propulsion of Bi_2WO_6 microswimmers was observed, confirming the successful synthesis of Bi_2WO_6 microswimmers.

4.4. Microplastic Degradation Efficiencies

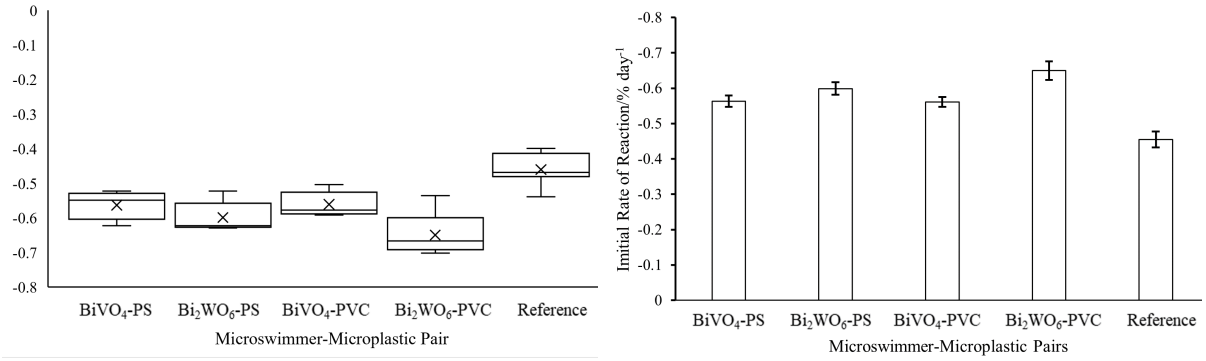

Figure 9. Graphs of (a) box and whisker plot and (b) bar graph of microplastic degradation efficiencies of all microswimmer-microplastic pairings. Whiskers in (a) represent Q_0 and Q_4. Q_1 and Q_3 are represented by the box. Q_2 is represented by the straight line.

From the raw data obtained, the derivative of each plot was obtained to obtain the rate of reaction due to each microswimmer. The initial rate of reaction was determined by the derivative of the degradation-time graph when day = 1.

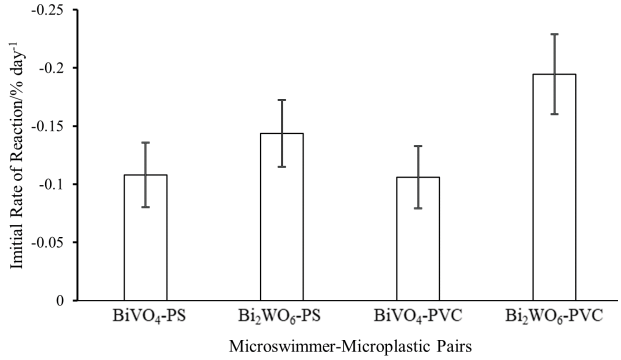

Figure 10. Bar graph of baseline-corrected microplastic degradation efficiencies of all microswimmer-microplastic pairings. Error bars are calculated by error propagation calculations of raw data and baseline data (reference).

The initial rate of reaction of the control was then subtracted from the derivative of each microswimmer to obtain the initial rate of change due to the microswimmers alone (Figure 10).

Statistical significance was obtained using the Mann-Whitney U Test on the initial rate of degradations. No significant difference was observed when comparing $BiVO_4$ and Bi_2WO_6 in their degradation of both polystyrene and polyvinyl chloride ($p = 0.174$ and $p = 0.0949$). The alternate hypothesis was thus rejected. Similarly, no significant difference was observed when comparing the degradation efficiency of $BiVO_4$ between polystyrene and polyvinyl chloride ($p = 1.00$) as well as when comparing the degradation efficiency of Bi_2WO_6 between polystyrene and polyvinyl chloride ($p = 0.0949$). The movement of the microswimmers is thus negligible in determining the rate of reaction with the microplastics. However, it could also be attributed to the fact that both microswimmers possess similar optical band gaps, thereby setting up local electric fields of equal magnitude and having similar electrophoretic mobilities (see Appendix B). Hence, the movement of microswimmers was indistinguishable. It can also be noted that the differing surface area to volume ratio of the microswimmers were insignificant as well.

As evident from Figure 10, there is a significant difference between the degradation efficiencies of microplastic when microswimmers are present in the solution. A significant difference in the

polystyrene degradation rates in the presence of $BiVO_4$ ($p = 0.0366$), and in the presence of Bi_2WO_6 ($p = 0.0214$) was confirmed. A significant difference in the polyvinyl chloride degradation rates in the presence of $BiVO_4$ ($p = 0.0214$), and in the presence of Bi_2WO_6 ($p = 0.0214$) was also confirmed. As stated in Appendix E, the presence of microswimmers provided another pathway for which the polymer chains in microplastics are degraded. In addition to the homolytic scission of C–C bonds due to the energy carried by visible light mentioned in Appendix D, microswimmers in the aqueous H_2O_2 solution had also generated hydroxyl radicals to attack the polymer chain to enhance the degradation of the microplastics.

4. Conclusion and Recommendations for Future Work

Characterisation of the microswimmers had shown that $BiVO_4$ microswimmers was successfully synthesised via the novel aqueous process. This method of synthesis was novel as it was the first non-hydrothermal reaction to form crystalline $BiVO_4$, without compromising the morphology or the optical band gap of the microspheres. Thus, production of $BiVO_4$ microspheres could become more efficient and without the need for a highly pressurised environment. Results and statistical analysis had concluded that the presence of microswimmers did increase the microplastic degradation efficiency of both PS and PVC microplastics. However, $BiVO_4$-Fe_3O_4 and Bi_2WO_6-Fe_3O_4 microswimmers showed no significant difference in microplastic degradation efficiency. This showed that both microswimmers are viable options for the degradation of microplastics in water, impacting research on the removal of plastics in drinking water. Moreover, this study has also shown that the addition of Fe_3O_4 on the microswimmers' surfaces was able to make them magnetic, without compromising the mobility. Therefore, this would increase the ease of use of microswimmers, enabling handlers to be able to magnetically remove and reuse the microswimmers after every use.

Limitations to this study include the duration of reaction for the synthesis of the microswimmers, as irregular morphology and aggregation was observed. This could have potentially affected the movement of the microswimmers and impacted the microplastic degradation efficiency. Hence, the reaction kinetics and duration of reaction should be optimised for future studies. In addition, future studies may investigate the effect of motion of microswimmers on microplastic degradation efficiency by varying the light intensity, which consequently affects the photocatalytic ability of the microswimmers.

References

Anglada, J. M., Crehuet, R., Martins-Costa, M., Francisco, J. S., & Ruiz-López, M. (2017). The atmospheric oxidation of CH_3OOH by the OH radical: the effect of water vapor. *Physical Chemistry Chemical Physics*, *19*(19), 12331-12342. http://dx.doi.org/10.1039/C7CP01976A

Borrelle, S. B., Ringma, J., Law, K. L., Monnahan, C. C., Lebreton, L., McGivern, A., ... & Rochman, C. M. (2020). Predicted growth in plastic waste exceeds efforts to mitigate plastic pollution. *Science*, *369*(6510), 1515-1518. https://doi.org/10.1126/science.aba3656

Bule Možar, K., Miloloža, M., Martinjak, V., Cvetnić, M., Kušić, H., Bolanča, T., ... & Ukić, Š. (2023). Potential of advanced oxidation as pretreatment for microplastics biodegradation. *Separations*, *10*(2), 132. https://doi.org/10.3390/separations10020132

Chia, R.W., Lee, J.Y., Kim, H. & Jang, J. (2021). Microplastic pollution in soil and groundwater: a review. *Environmental Chemistry Letters*, *19*, 4211-4224. https://doi.org/10.1007/s10311-021-01297-6

Delice, S., Isik, M., & Gasanly, N. M. (2024). Temperature-dependent tuning of band gap of Fe_3O_4 nanoparticles for optoelectronic applications. *Chemical Physics Letters*, *840*, 141139. https://doi.org/10.1016/j.cplett.2024.141139

Deng, Y., & Zhao, R. (2015). Advanced oxidation processes (AOPs) in wastewater treatment. *Current Pollution Reports*, *1*, 167-176. https://doi.org/10.1007/s40726-015-0015-z

Ding, L. L., Zhao, Q., Zhu, J. L., Fan, Z. J., & Liu, B. (2016, March). The preparation and property research of bismuth oxide nanospheres. In *International Conference on Materials Chemistry and Environmental Protection 2015* (pp. 17-20). Atlantis Press. https://doi.org/10.2991/meep-15.2016.5

Hong, Y., Blackman, N. M., Kopp, N. D., Sen, A., & Velegol, D. (2007). Chemotaxis of nonbiological colloidal rods. *Physical review letters*, *99*(17), 178103. https://doi.org/10.1103/PhysRevLett.99.178103

Khairudin, K., Bakar, N. F. A., & Osman, M. S. (2022). Magnetically recyclable flake-like BiOI-Fe_3O_4 microswimmers for fast and efficient degradation of microplastics. *Journal of*

Environmental Chemical Engineering, *10*(5), 108275. https://doi.org/10.1016/j.jece.2022.108275

Kibria, Md. G., Masuk, N. I., Safayet, R., Nguyen, H. Q., & Mourshed, M. (2023). Plastic Waste: Challenges and Opportunities to Mitigate Pollution and Effective Management. *International Journal of Environmental Research*, *17*, 20. https://doi.org/10.1007/s41742-023-00507-z

Kudo, A., Omori, K., & Kato, H. (1999). A novel aqueous process for preparation of crystal form-controlled and highly crystalline $BiVO_4$ powder from layered vanadates at room temperature and its photocatalytic and photophysical properties. *Journal of the American Chemical Society*, *121*(49), 11459-11467. https://doi.org/10.1021/ja992541y

Liu, X., Wang, S., Wang, S., Shi, H., Zhang, X., & Zhong, Z. (2019). The three-dimensional flower-like Bi_2WO_6 assisted by ethanolamine through a microwave method for efficient photocatalytic activity. *Royal Society Open Science*, *6*(3), 181422. https://doi.org/10.1098/rsos.181422

Pookmanee, P., Kojinok, S., Puntharod, R., Sangsrichan, S., & Phanichphant, S. (2013). Preparation and Characterization of $BiVO_4$ Powder by the Sol-gel Method. *Ferroelectrics*, *456*(1), 45–54. https://doi.org/10.1080/00150193.2013.846197

Ricardo, I. A., Alberto, E. A., Júnior, A. H. S., Macuvele, D. L. P., Padoin, N., Soares, C., ... & Trovo, A. G. (2021). A critical review on microplastics, interaction with organic and inorganic pollutants, impacts and effectiveness of advanced oxidation processes applied for their removal from aqueous matrices. *Chemical Engineering Journal*, *424*, 130282. https://doi.org/10.1016/j.cej.2021.130282

Sharifinia, M., Bahmanbeigloo, Z.A., Keshavarzifard, M., Khanjani, M.H. & Lyons, B.P. (2020). Microplastic pollution as a grand challenge in marine research: A closer look at their adverse impacts on the immune and reproductive systems. *Ecotoxicology and Environmental Safety*, *204*. https://doi.org/10.1016/j.ecoenv.2020.111109

Wang, L., Kaeppler, A., Fischer, D. & Simmchen, J. (2019). Photocatalytic TiO_2 Micromotors for Removal of Microplastics and Suspended Matter. *ACS Applied Materials and Interfaces*, *11*, 32579-33524. https://doi.org/10.1021/acsami.9b06128

Wang, R., Jiang, Z., Xu, L., & Liu, C. (2021). Synthesis of Dy (III) doped Bi_2WO_6 photocatalyst with highly efficient photocatalytic performance under simulated sunlight. *Journal of Materials Science: Materials in Electronics*, *32*, 6931-6941. https://doi.org/10.1007/s10854-021-05399-3

Yu, X., Wang, Z., Li, E., Li, X., Cui, M., & Guo, C. (2022). Preparation of different BiVO4 catalysts and their photocatalytic performance in the coupling reaction between alcohols and amines. *Catalysis Letters*, *152*(4), 1244-1255. https://doi.org/10.1007/s10562-021-03713-6

Zhan, X., Wang, J., Xiong, Z., Zhang, X., Zhou, Y., Zheng, J., ... & Tang, J. (2019). Enhanced ion tolerance of electrokinetic locomotion in polyelectrolyte-coated microswimmer. *Nature communications*, *10*(1), 3921. https://doi.org/10.1038/s41467-019-11907-1

Appendices

Appendix A: Tauc Plot and Determination of Band Gap

The Tauc Method relies on the assumption that the coefficient of absorbance, α, can be expressed using the Tauc equation:

$$(\alpha \cdot h\nu)^{1/\gamma} = B(h\nu - E_g)$$

where h is the Planck constant (approx. 6.626e-24), ν is the photon frequency, with $h\nu$ thus representing the energy of a given incident wave. B is the band tailing parameter. γ is the nature of the electron transition band gap (½ when direct, 2 when indirect). E_g is the band gap.

A Tauc Plot is a graph of $(\alpha \cdot h\nu)^{1/\gamma}/cm^{1/\gamma}$ $h\nu/eV$. Rewriting Eq. 1:

$$(\alpha \cdot h\nu)^{1/\gamma} = B(h\nu) - B(E_g)$$

which is in the form $y = mx + c$.

When $(\alpha \cdot h\nu)^{1/\gamma} = 0$ (i.e. at the x-axis),

$$B(h\nu) = B(E_g)$$

Dividing both sides by B,

$$h\nu = E_g$$

Therefore, the intersection of a fitted line with the Tauc Plot, will represent the bandgap of a material. This also makes intuitive sense. The rise in the Tauc Plot is due to a rise in absorbance in a UV-Vis Spectra. When absorbance increases, there is enough energy in the incident waves to excite electrons from the valence band, to the conduction band, through the band gap. Similarly, when electrons are excited, there will be an increase in the Tauc Plot. The abscissa where the plot starts increasing, therefore shows the band gap/energy gap.

Due to the presence of Urbach Tails in UV-Vis Spectrums, there also exists non-zero absorbance below E_g. To account for this, the portion of linear increase in the Tauc Plot was extrapolated , so as to identify the point when absorbance increases.

Extrapolating the linear portion of the Tauc Plot to the x-axis, E_g, the band gap was then identified.

Appendix B: Movement of Microswimmers

Microswimmers utilise their high band gaps and photocatalytic properties to assist in their motion through a liquid medium via self-electrophoresis.

In the presence of visible light or ultraviolet light, Electron-hole pairs were formed within the microswimmer. Electrons in $BiVO_4$ and Bi_2WO_6 were excited to produce positive holes in the valence band with an oxidative capacity, which concurrently leaves negative electrons at the conduction band with a reductive capacity (Deng & Zhao, 2015):

$$BiVO_4 + hv \rightarrow hv_{vb}^{+} + e_{cb}^{-}$$

The electrons and holes are then capable of reacting with H_2O and O_2 molecules which are absorbed on the semiconductor surface as H_2O_2 decomposes to form negative and positive charged species:

$$hv_{vb}^{+} + H_2O \rightarrow \bullet OH + H^{+}$$

$$e_{cb}^{-} + O_2 \rightarrow O_2^{\bullet -}$$

On the hemisphere where photons excite the electrons in the microswimmer, positive H^+ ions will be accumulated whereas negative $O_2^{\bullet -}$ will accumulate on the opposing hemisphere. Thus, the unbalanced ions will set up a local spatially uniform electric field to initiate self-propulsion of the microswimmer (Zhan et al., 2019). The direction of motion appears to be random and similar to that of brownian motion due to the combination of the electrophoretic propulsion and rotational diffusion of the microswimmer (Hong et al., 2007).

Appendix C: Microplastic Degradation Pathway

AOPs have been shown to be promising strategies for the degradation of microplastics, especially from aqueous matrices.

AOPs are based upon the generation of sulphate or hydroxyl radicals which have high standard reduction potential or the tendency to be reduced (+2.6eV for $SO_4^{\bullet -}$ and +2.8eV for •OH at pH 0). Thus, these radicals are extremely reactive oxidising agents and nonselective in their behaviours to react rapidly with organic and inorganic pollutants (Ricardo et al., 2021).

Appendix D: Microplastic Degradation in Control Set-up

As most organic polymers such as PS and PVC are sensitive to irradiation in the visible light and UV spectrum, the energy carried by the visible light is able to cause the homolytic fission of the C–C bonds in the polymer, producing carbon-centred polymer radicals ($R\bullet$) (Možar et al., 2023):

$$R_2 + hv \rightarrow 2R\bullet$$

The amount of energy carried by the light may also be great enough to cause the abstraction of a hydrogen atom from a hydrocarbon in the polymer chain, forming a carbon-centred polymer radical:

$$RH + hv \rightarrow R\bullet + H\bullet$$

Then, the highly reactive hydrogen radical will react with hydrocarbons at another site of the polymer chain to abstract yet another hydrogen atom:

$$RH + H\bullet \rightarrow R\bullet + H_2$$

In the presence of oxygen molecules, the carbon-centred radicals will react and form peroxyl radicals which will react with hydrocarbons at another site of the polymer chain to form hydroperoxide groups:

$$R\bullet + O_2 \rightarrow ROO\bullet$$

$$ROO\bullet + RH \rightarrow ROOH + R\bullet$$

In the case of PS, the carbon-centred polymer radical will be CH_2, and the ROOH hydroperoxide group will hence be CH_2OOH, which dissociates to form formaldehyde gas and aqueous hydroxide ions, effectively degrading the microplastic into soluble or gaseous compounds (Anglanda et al., 2017):

$$CH_2OOH \rightarrow H_2CO(g) + OH^-(aq)$$

$$H_2CO/O \rightarrow H_2 + CO_2$$

Appendix E: Microplastic Degradation in Independent Set-ups

As hydroxyl radicals produced via the decomposition of H_2O_2 approaches the microplastics, they will attack the polymer chains by reacting with the organic compound to form carbon-centred radicals:

$$OH\bullet + RH \rightarrow R\bullet + H_2O$$

$$R\bullet + OH \rightleftharpoons R\bullet\text{–}OH$$

As more peroxyl radicals are formed, the position of equilibrium shifts to the left to reduce the decrease in concentration of carbon-centred radicals.

In the presence of oxygen molecules, the carbon-centred radicals will react and form peroxyl radicals which will react with hydrocarbons at another site of the polymer chain to form hydroperoxide groups:

$$R\bullet + O_2 \rightarrow ROO\bullet$$

$$ROO\bullet + RH \rightarrow ROOH + R\bullet$$

In the case of PS, the carbon-centred polymer radical will be CH_2, and the ROOH hydroperoxide group will hence be CH_2OOH, which dissociates to form formaldehyde gas and aqueous hydroxide ions, effectively degrading the microplastic into soluble or gaseous compounds:

$$CH_2OOH \rightarrow H_2CO(g) + OH^-(aq)$$

Appendix F: Photographs of Photoreactor

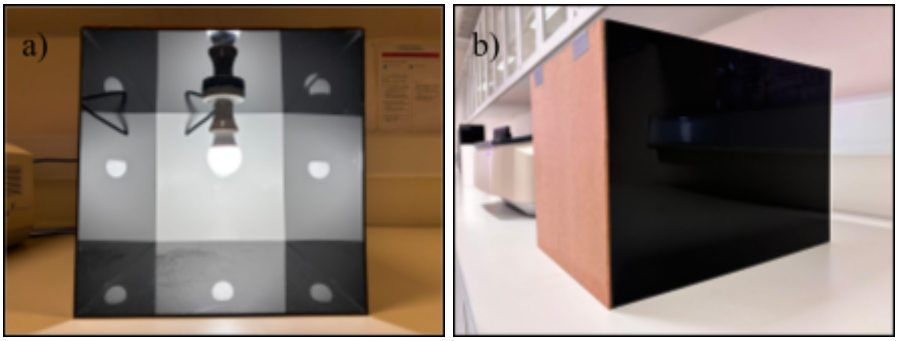

Figure F1. (a) Front view and (b) side view of constructed photoreactor

Appendix G: Photograph of Experimental Set-ups

Figure G1. Front view of experimental set-ups

Appendix H: Microswimmers under Microscope Magnification

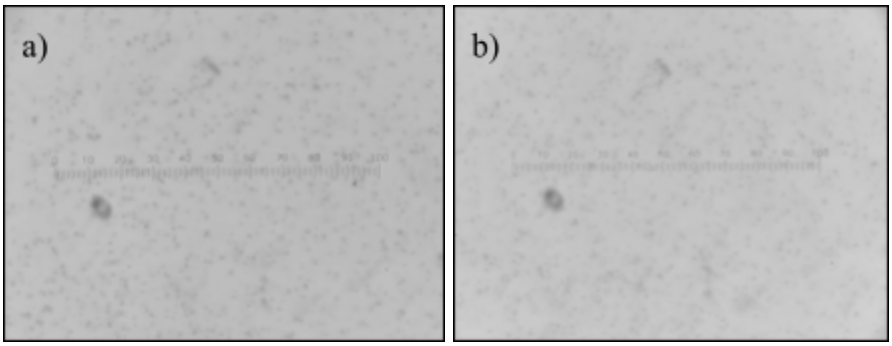

Figure H1. 100x microscope view of (a) $BiVO_4$ and (b) Bi_2WO_6